

Article

Tuning the Structure and Acidity of Pt/Hierarchical SSZ-32 Catalysts to Boost the Selective Hydroisomerization of *n*-Hexadecane

Xinyue Yang ^{1,2}, Wenli Zhao ^{1,2}, Linlin Liu ^{1,2}, Xiaopo Niu ^{1,2} and Qingfa Wang ^{1,2,3,*}

¹ Key Laboratory for Green Chemical Technology of Ministry of Education, School of Chemical Engineering and Technology, Tianjin University, Tianjin 300072, China

² Collaborative Innovation Center of Chemical Science and Engineering (Tianjin), Tianjin University, Tianjin 300072, China

³ Zhejiang Institute of Tianjin University, Ningbo 315201, China

* Correspondence: qfwang@tju.edu.cn; Tel.: +86-22-27892340

Abstract: Developing highly selective and efficient bifunctional catalysts is an important issue for the hydroisomerization of long-chain *n*-alkanes. It is vital to tailor the balance of isomerization and cracking reactions in hydroisomerization. Herein, a bifunctional Pt/hierarchical SSZ-32 catalyst was fabricated with a sequential desilication–dealumination treatment to boost the selective hydroisomerization of *n*-hexadecane (C₁₆). The pore structure and acid sites of SSZ-32 zeolite were tailored. More mesopore and Brønsted acid sites were generated, and the ratio of weak to strong Brønsted acidity (B_w/B_s) was increased by the sequential desilication–dealumination. The generated hierarchical structure had little effect on the selectivity of the reaction pathways of hydroisomerization versus cracking. The ratio of isomers/cracking products increased almost linearly with the increase in the B_w/B_s ratios. Meanwhile, the synergetic effect of the hierarchical structure and acidity regulation promoted the selectivity of monobranched *i*-C₁₆ products. Therefore, the resulting Pt/SSZ-0.6AS exhibited the highest activity with a total isomer yield of 71.5% at 255 °C and the enhanced formation mechanism of monobranched isomers occurred via the pore mouth.

Keywords: hierarchical SSZ-32 zeolites; bifunctional catalysts; *n*-hexadecane hydroisomerization; Brønsted acidity distribution; reaction pathways



Citation: Yang, X.; Zhao, W.; Liu, L.; Niu, X.; Wang, Q. Tuning the Structure and Acidity of Pt/Hierarchical SSZ-32 Catalysts to Boost the Selective Hydroisomerization of *n*-Hexadecane. *Catalysts* **2023**, *13*, 702. <https://doi.org/10.3390/catal13040702>

Academic Editors: Maja Milojević-Rakić and Danica Bajuk-Bogdanović

Received: 26 February 2023

Revised: 31 March 2023

Accepted: 3 April 2023

Published: 5 April 2023



Copyright: © 2023 by the authors. Licensee MDPI, Basel, Switzerland. This article is an open access article distributed under the terms and conditions of the Creative Commons Attribution (CC BY) license (<https://creativecommons.org/licenses/by/4.0/>).

1. Introduction

The hydroisomerization of long-chain *n*-alkanes plays an important role in the petroleum industry, in which heavy distillate and residue are converted into value-added products, such as gasoline, jet fuel, and lubricant oils [1]. The branching of *n*-alkanes through hydroisomerization is one strategy to improve the octane number of gasoline and to enhance the performance of diesel or lubricating oils at low temperatures [2,3]. It is agreed that the hydroisomerization reaction is always accompanied by a side reaction of hydrocracking, resulting in a much lower selectivity and yield of isomers than 100%, especially for the long-chain alkanes, which maintain a high tendency towards cracking [4]. Therefore, boosting the selectivity of hydroisomerization by controlling the cracking reaction is a very necessary and severe challenge. How to construct efficient and excellent hydrogen isomerization catalysts for *n*-alkanes to maintain high selectivity of isomeric alkanes and low cracking rate has always been the focus of research. Many works have been carried out to achieve a better balance of hydroisomerization and cracking reactions by regulating their reaction pathways. Unfortunately, there is still a lack of comprehensive understanding on how to tailor the reaction pathways in the hydroisomerization of *n*-alkanes.

Traditionally, metal–acid bifunctional catalysts are used for the hydroisomerization of *n*-alkanes, which undergo hydrogenation/dehydrogenation on metallic sites (usually Pt or

Pd) and protonation/deprotonation and skeleton rearrangement on acidic sites [5–9]. In the hydroisomerization of n -C₈ to n -C₁₆ alkanes, silicoaluminophosphate and aluminosilicate molecular sieves, such as SAPO-11 [10], ZSM-22 [11–14], ZSM-23 [15,16], ZSM-48 [17], and SSZ-32 [18,19], are commonly used as the support of the bifunctional catalysts for shape-selective hydroisomerization [20–22]. Recently, SSZ-32 (0.45 nm × 0.52 nm) zeolite with a unique MTT structure and one-dimensional pores has attracted more attention in the hydroisomerization of long-chain n -alkanes because of its intrinsic microporous framework structure, suitable acid sites, high hydrothermal stability, environmental friendliness, and good shape selectivity [20]. In addition, compared with ZSM-23 zeolite, SSZ-32 has been considered to be superior for the hydrodewaxing of long-chain alkanes with good selectivity and smaller crystal size, which has many advantages in applied catalysis fields [23], such as producing lubricant base oils from Fischer–Tropsch wax [24]. The activity and selectivity of hydroisomerization are directly affected by the textural properties and acidity of supports, particle dispersion and reductivity of metal centers, and the metal–acid balance [6]. Many approaches have been developed to alter pore structure and acidity distribution. For example, a series of SAPO-11 molecular sieves were synthesized in an alcohol–water concentrated gel system with improved acidity and mesoporous volume and were used as the support for the hydroisomerization of n -hexadecane [25]. Liang et al. synthesized ZSM-23 zeolites with dual-structure directing agents and Fe-substituted ZSM-23 for the hydroisomerization of n -hexadecane [26,27]. In our previous work, we developed a partial detemplation method to investigate the influence of pore structure and acidity of Pt/ZSM-22 catalysts on the hydroisomerization of n -dodecane [20]. Post-synthetic treatments, such as desilication, dealumination, and sequential post-synthetic treatment, are an effective approach, and many zeolites have been widely used (ZSM-5, H β , HY, USY, SAPO-11, ZSM-48, H-ZSM-22, ZSM-23, and so on) for hydrogenation and hydroisomerization [28–31]. The alkali-treated and acid-treated ZSM-23-supported Pt bifunctional catalysts exhibited an outstanding n -C₁₆ hydroisomerization performance, with the highest i -C₁₆ yield of 64 wt.% at 340 °C [32]. The alkali–acid-treated hierarchical Pt/ZSM-22 zeolites with 0.3 M NaOH and with 6.0 M HCl and 0.1 M H₂SiF₆ exhibited 81.1% of the highest n -heptane conversion and 76.4% of total i -heptane yield at 260 °C [33]. Zhou et al. post-treated ZSM-5 zeolite with ammonium hexafluorosilicate (AHFS) and potassium carbonate (K₂CO₃) to control pore structure and acidity. They revealed that the use of AHFS and K₂CO₃ post-treatment resulted in the production of more mesopores to boost the diffusion of aromatic products and reduced the strength of strong acid sites in ZSM-5 to prevent excessive cracking reactions [34]. Wang et al. prepared hierarchical HY molecular sieves with good hierarchical structure by alkali treatment, which efficiently promoted the directional alkylation of naphthalene and cyclohexene catalytic reaction. The poriness and acidity of HY zeolite were optimized to increase the accessibility to active acid sites by regulating the concentration of NaOH, resulting in the hierarchical 0.5 HY zeolite with good catalytic activity and cycle stability [35]. However, studies reporting the roles of pore structure and acidity of SSZ-32 zeolite on the hydroisomerization of alkanes are rare. Introducing the secondary mesoporous networks into SSZ-32 molecular sieves with unique pore structures can effectively enhance the diffusion efficiency, expose more active sites, and improve the accessibility of acid sites, which is critical to explore the influence of textural properties and acidity on the reaction pathways of isomerization/cracking.

In this context, we tailored the textural properties and acidity of hierarchical SSZ-32 zeolites by desilication and sequential desilication–dealumination treatments. The catalytic hydroisomerization of long-chain n -alkanes over these post-treated SSZ-32-supported Pt catalysts was systematically carried out. The aim was to reveal the influence of the hierarchical structure as well as acid strength and distribution on the reaction pathways of isomerization/cracking and the formation mechanism of monobranched isomers.

2. Results and Discussion

2.1. Structure and Morphology of Pt/Hierarchical SSZ-32 Catalysts

The skeleton structure of the parent and post-treated SSZ-32 zeolites were determined by XRD characterization. As shown in Figure 1, all the samples showed a typical MTT topological structure with six distinct characteristic diffraction peaks at $2\theta = 8.1^\circ$, 11.3° , 19.7° , 20.9° , 22.9° , and 24.0° (PDF# 37-0411). The Si/Al ratio decreased from 20.6 to 17.4 for SSZ32-0.3A and 14.3 for SSZ32-0.6A due to the desilication by alkali treatment, while after acid treatment, the Si/Al ratio of the alkali–acid-treated samples increased significantly, ascribed to the removal of extra-framework species. The relative crystallinity (RC) of all samples was calculated and the results are listed in Table 1. The relative crystallinity of the desilicated SSZ-32 samples decreased significantly with the increase in alkali concentration due to the partial collapse of the skeleton structure and the formation of the amorphous phase. However, the relative crystallinity of the SSZ32-0.3AS and SSZ32-0.6AS samples was partially recovered owing to the removal of the amorphous phase by the sequential acid leaching. This was confirmed by TEM characterization. The parent SSZ-32 zeolite showed a smooth external surface and complete rod-like morphology with a nanorod diameter around 20 nm. Meanwhile, certain intercrystalline voids were observed because of the accumulation of SSZ-32 nanorods. After being treated by weak desilication, the morphology and structure of SSZ32-0.3A and SSZ32-0.3AS samples remained nearly intact. A small number of mesopores were observed at the edge of the rod-like crystals in these samples. Compared with the SSZ32-0.3A sample, no crystal fragments were found on the surface of the SSZ32-0.3AS sample, confirming that the crystal fragments generated during the alkali treatment were removed by acid leaching. For the SSZ32-0.6A sample, the amount and size of mesopores increased significantly, and more crystal fragments were generated, while for the SSZ32-0.6AS sample, most of the crystal fragments were removed, and more and larger mesopores were formed. Mavrodinova et al. believed that extra lattices could be removed from the molecular sieve structure by acid reflux [36], thus, improving the accessibility of the inherent micropores of the molecular sieve. These results indicated that the mesopore was generated after the desilication treatment, and the sequential alkali–acid treatment could help to remove crystal fragments and amorphous phases, which further promoted the diffusion of reactants and improved the accessibility of acid sites in zeolite.

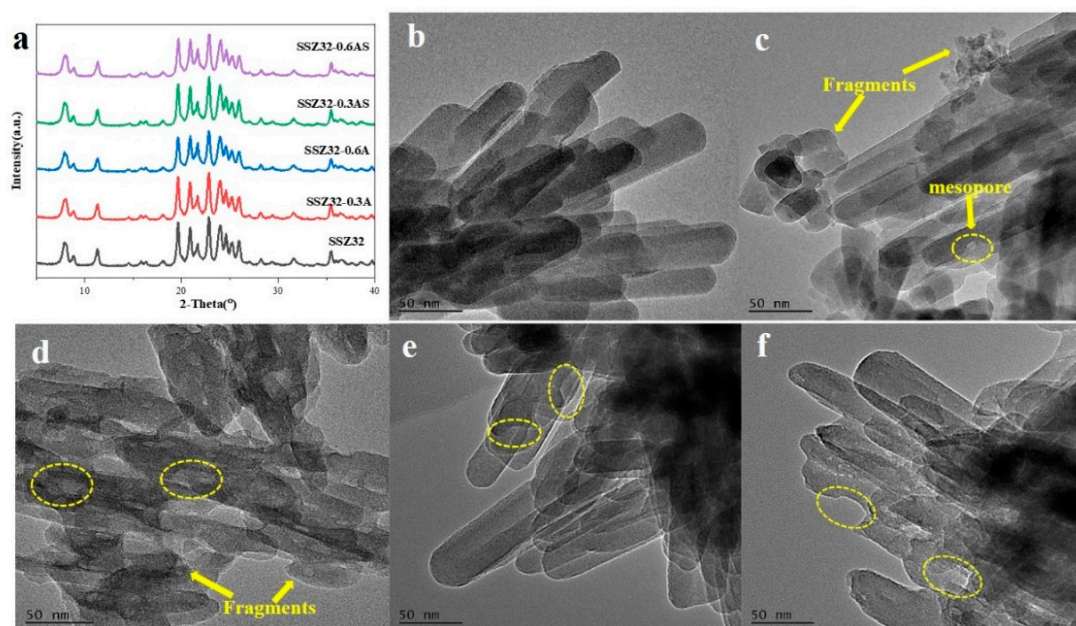


Figure 1. XRD patterns (a) and TEM images of parent SSZ32 (b) and post-treated SSZ32-0.3A (c), SSZ32-0.6A (d), SSZ32-0.3AS (e), and SSZ32-0.6AS (f).

Table 1. Textural properties for parent and hierarchical SSZ-32-supported Pt catalysts.

Samples	RC ^a (%)	Specific Surface Area (m ² /g)			Volume (cm ³ /g)		
		S _{BET}	S _{micro}	S _{meso}	V _{total}	V _{micro}	V _{meso}
Pt/SSZ32	100	103.73	71.65	32.08	0.158	0.0400	0.118
Pt/SSZ32-0.3A	95.5	92.92	42.05	50.87	0.147	0.0203	0.127
Pt/SSZ32-0.6A	84.7	98.50	33.48	65.01	0.162	0.0184	0.144
Pt/SSZ32-0.3AS	99.7	134.85	62.30	72.55	0.178	0.0271	0.151
Pt/SSZ32-0.6AS	88.6	160.75	68.63	92.12	0.218	0.0342	0.184

^a Determined by XRD.

To further understand the textural structure of the parent and alkali-/acid-treated catalysts, the pore size distribution was determined by conducting the N₂ isothermal adsorption–desorption curve. As shown in Figure 2, the parent SSZ32 zeolite showed a typical type-I isotherm profile with a rapid uptake at very low relative pressure of $p/p_0 < 0.02$ and an adsorption saturation platform at high relative pressure, which exhibited the characteristic of a microporous structure. Additionally, an obvious uptake at the relative pressure of $p/p_0 = 0.9–0.99$ and a faint hysteresis was also shown in the parent sample, indicating the existence of mesopores caused by the stacked gaps or voids [18,37]. Compared with the parent SSZ-32, all the alkali-/acid-treated catalysts showed a typical type-VI isotherm with a hysteresis in the relative pressure range of $p/p_0 = 0.4–0.99$, suggesting the formation of mesopores. The hysteresis became more and more obvious with the increase in the desilication degree. This indicated that micro-mesopore hierarchical structures were formed and more intracrystalline mesopores were generated by high-concentration alkali treatment. In addition, the uptake at the relative pressure of $p/p_0 < 0.1$ decreased gradually with the increase in desilication degree. The Pt/SSZ32-0.6A catalyst showed the lowest uptake at low relative pressure ($p/p_0 < 0.1$) and more obvious hysteresis at high relative pressure, indicating that more mesopores were generated with the decrease in micropores. After acid leaching, the uptake of alkali-treated samples at $p/p_0 < 0.1$ was significantly enhanced and a bigger hysteresis was obtained, which indicated that more micropores and mesopores blocked by the dissolved fragment were recovered. The pore size distribution derived from the BJH adsorption branch is plotted in Figure 2b. The intercrystalline mesopore in the Pt/SSZ32 was centered at 25 nm. After alkali treatment, the average mesopore size significantly increased up to 30 nm for Pt/SSZ32-0.3A and 40 nm for Pt/SSZ32-0.6A because of the generation of a large number of mesopores. With additional acid treatment, the mesopore size further increase slightly by about 3 nm due to the removal of leached extra-framework oxides. Additionally, the signal strength also increased significantly with the increase in desilication degree from alkali treatment, and further increased after acid treatment, especially for the Pt/SSZ32-0.6AS. This indicated that the content of mesopore increased significantly. As listed in Table 1, the parent SSZ32-supported Pt catalyst (Pt/SSZ32) showed a BET-specific surface area (S_{BET}) of 103.73 m²/g with a S_{micro} value of 71.65 m²/g, indicating the microporous characteristic of a SSZ-32 support. With the increase in alkali concentration, the S_{micro} value of alkali-treated catalysts decreased significantly with an increase in S_{meso} value. The S_{BET} value first showed a decrease for Pt/SSZ32-0.3A and then an increase for Pt/SSZ32-0.6A because of the significant increase in S_{meso} value. Additionally, the mesopore volume significantly increased from 0.118 cm³/g for Pt/SSZ32 to 0.127 cm³/g for Pt/SSZ32-0.3A and 0.144 cm³/g for Pt/SSZ32-0.6A. After further acid treatment, the total S_{BET} value increased significantly with the increase in S_{micro} and S_{meso} values, especially for Pt/SSZ32-0.6AS with a high S_{micro} value (68.63 m²/g) and S_{meso} value (92.12 m²/g). Consequently, the mesopore volume of Pt/SSZ32-0.6AS increased significantly, up to 0.184 cm³/g, derived from the quick increase of generated mesopores. In the alkali treatment, internal Si-OH groups of the zeolite were partially dissociated, and part of the micropores were etched to form the mesopores located on the external surface of the crystal structure or in the defect regions. Within the molecular sieve framework, the reaction occurred between the hydroxide anions (OH⁻) and the silanol groups (defect sites).

The alkali metal cation stabilized the extracted silicate anions, leading to voids within the skeleton. The Na⁺ ion is the best leaching agent for silicon atoms because of its excellent ability to stabilize silicate anions [38]. In the meantime, partial framework Al species are usually removed and deposited on the external surface of the zeolite in the form of amorphous etched oxides to block part of the pore mouth, which resulted in the significant decrease in S_{micro} and V_{micro} values. Simultaneously, the V_{micro} values of Pt/SSZ32-0.3AS and Pt/SSZ32-0.6AS were still smaller than that of the Pt/SSZ32 because of the transformation of micropores into mesopores. These results indicated that the acid treatment of desilicated SSZ-32 in sequential alkali–acid treatment plays a vital role in recovering the pore surface area and volume by significantly removing the etched oxide species.

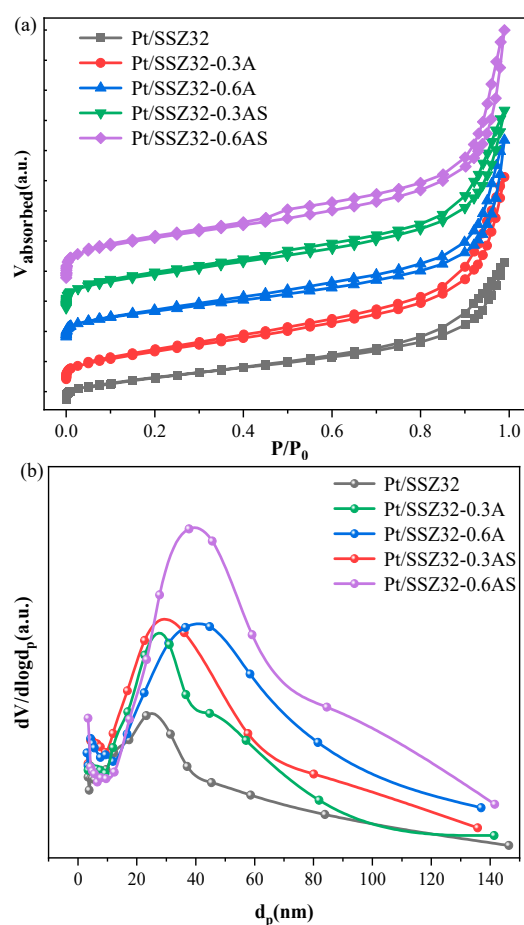


Figure 2. N_2 adsorption–desorption isotherm (a) and pore size distribution (b) of parent and hierarchical SSZ-32-supported Pt catalysts.

The chemical environment and coordination of Al species in all the samples were characterized by ^{27}Al MAS NMR. As shown in Figure 3, a sharp peak at ca. 57 ppm was observed in all the catalysts, which could be assigned to framework tetrahedral coordination Al species (FAI). A weak peak at 0 ppm assigned to extra-framework Al (EFAl) species was also observed. In the meantime, the framework Al signal at ≈ 57 ppm of the Pt/SSZ32- x A(S) samples showed a broad shoulder resonance extending to the upfield. This broadening might be associated with the distorted tetrahedral Al atoms (40–50 ppm region, Figure 3) [39–41]. The coordination environmental distribution of Al species was further calculated and listed in Table 2. The Pt/SSZ32 had a FAI content of 83.6% with a small number of distorted FAI species (6.1%) and EFAl species (10.3%). The EFAl species in this sample were probably generated from the conversion of the tetrahedrally coordinated framework Al at a high calcination temperature [42]. With the increase in alkali concentration, the framework and distorted framework Al species of the desilicated

samples decreased with the significant increase in extra-framework Al species, up to 14% for Pt/SSZ32-0.3 and 24.8% for Pt/SSZ32-0.6A. The increased extra-framework Al species might have resulted in the channels in the zeolites becoming blocked [43]. After further acid treatment, the extra-framework Al species was obviously removed. The content of EFAl species decreased to 10.8% for the Pt/SSZ32-0.3AS sample. However, for the Pt/SSZ32-0.6AS sample, only 5.2% EFAl species was observed, indicating the removal of most extra-framework Al species. Part of the distorted framework Al species was converted into the framework Al species in the Pt/SSZ32-0.3AS sample. In contrast, part of the framework Al species was converted into the distorted framework Al species in the Pt/SSZ32-0.6AS sample. This indicated that in the process of the sequential alkali–acid treatment, acid treatment could not only remove the fragment and the generated extra-framework Al species in the alkali treatment, but also alter the distribution of framework and distorted framework Al species.

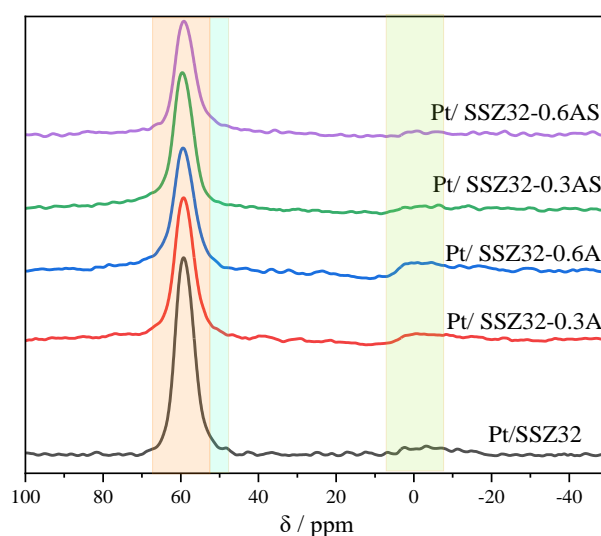


Figure 3. ^{27}Al MAS NMR spectra of parent and hierarchical SSZ-32-supported Pt catalysts.

Table 2. Quantitative analysis of Al proportions in different coordination states based on ^{27}Al MAS NMR spectra.

Catalysts	The Proportion of Different Al Species			Si/Al
	FAI % (57 ppm)	Distorted FAI (~52 ppm)	EFAl % (0 ppm)	
Pt/SSZ32	83.6	6.1	10.3	20.6
Pt/SSZ32-0.3A	80.6	5.4	14.0	17.4
Pt/SSZ32-0.6A	71.5	3.7	24.8	14.3
Pt/SSZ32-0.3AS	85.4	3.8	10.8	22.5
Pt/SSZ32-0.6AS	85.9	8.9	5.2	19.6

Acidity Properties

The acidity of different catalysts was determined by Py-FTIR and NH_3 -TPD. To quantify the acid sites of zeolites after alkali treatment and sequential alkali–acid treatment, the Py-FTIR spectra at different temperature were obtained. As shown in Figure 4, the characteristic peaks at 1545 cm^{-1} and 1450 cm^{-1} belonged to the absorption vibration of pyridine adsorbed on the Brønsted acid sites (BAS) and Lewis acid sites (LAS). The quantitative analysis of Brønsted acidity (B) and Lewis acidity (L) was conducted according to the spectra measured at $200\text{ }^\circ\text{C}$ and $350\text{ }^\circ\text{C}$, and the results are listed in Table 3. The Pt/SSZ32 catalyst showed a high B/L ratio (1.85) with a total acidity of $133.8\text{ }\mu\text{mol/g}$ and a high ratio of strong BAS to strong LAS, indicating the dominance of BAS. As for the alkali-treated samples, the Brønsted and total acidity decreased with the increased Lewis

acidity, especially the strong Lewis acidity. In addition, it can be observed that the decrease in total Brønsted acidity mainly came from the reduction in strong Brønsted acidity for Pt/SSZ32-0.3A. However, for Pt/SSZ32-0.6A, the decrease in total Brønsted acidity came from the decrease in weak Brønsted acidity. The change in acid sites was attributed to the partial destruction of the SSZ-32 microporous framework and the formation of mesoporous structure, generating the more accessible extra-framework Al and Si species. The generated extra-framework Al species was the precursor of LAS, which promoted the formation of acid sites directly and gave rise to Lewis acidity [44,45], and the B acidity was derived from the framework Al species [45]. As a result, the total acidity and the B/L ratio for the alkali-treated samples decreased, especially the ratio of strong B acid sites to strong L acid sites. After further acid treatment, more BAS sites were generated on the alkali-acid-treated catalyst with fewer LAS sites. This could be attributed to the formation of mesopores exposing more framework acid sites. Additionally, the Brønsted acidity and total acidity were increased and reached a maximum on the Pt/SSA32-0.6AS, and the increase in Brønsted acidity mainly derived from the strong Brønsted acidity for the Pt/SSA32-0.3AS but switched from the weak Brønsted acidity for Pt/SSA32-0.6AS. The Lewis acidity did not show an obvious change, probably due to the similar total extra-framework and distorted FAI species, both of which were the LAS [44]. Moreover, the B/L ratios significantly increased up to 2.44 for Pt/SSA32-0.3AS and 3.54 for Pt/SSA32-0.6AS, elucidating that Brønsted acidity contributed more to the total acidity for the alkali-acid-treated catalysts.

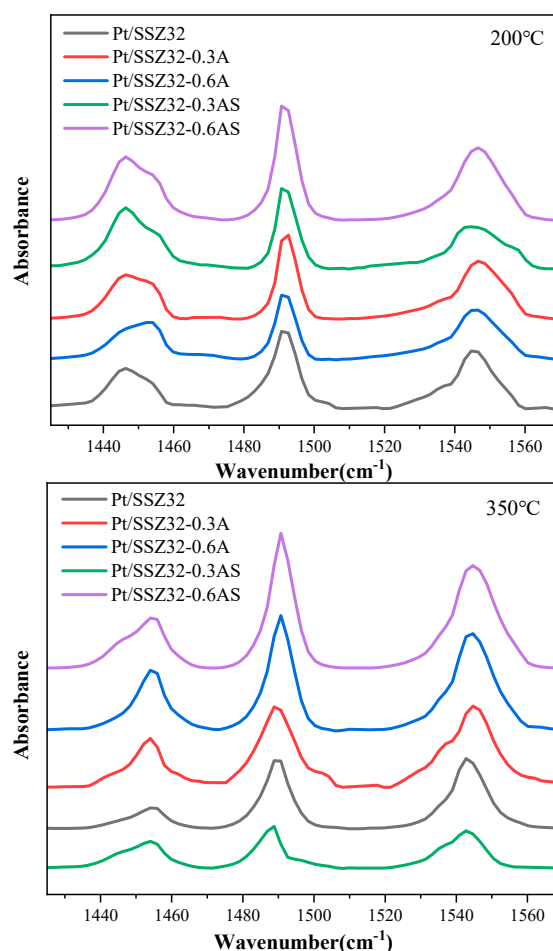
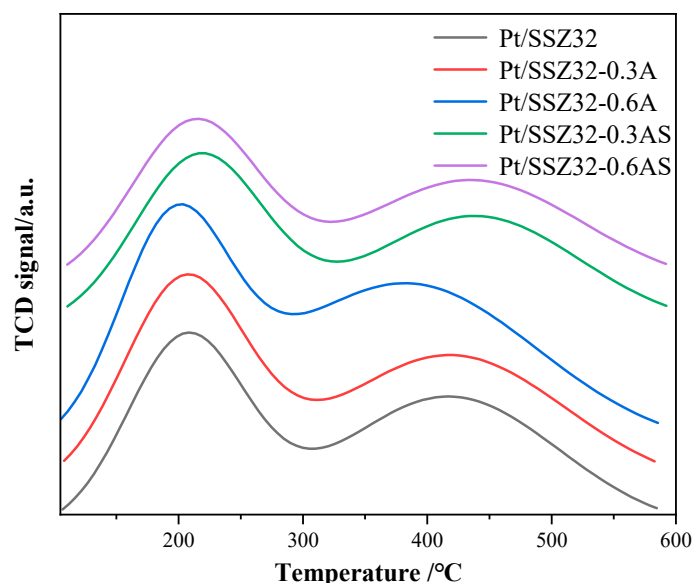


Figure 4. FTIR spectra of pyridine adsorption on parent and hierarchical SSZ-32-supported Pt catalysts.

Table 3. Acidity of parent and hierarchical SSZ-32-supported Pt catalysts determined by Py-FTIR spectra.

Samples	Brønsted Acidity ($\mu\text{mol g}^{-1}$)		Lewis Acidity ($\mu\text{mol g}^{-1}$)		Total Acidity ($\mu\text{mol g}^{-1}$)		B/L Ratio	
	200 °C	350 °C	200 °C	350 °C	200 °C	350 °C	200 °C	350 °C
Pt/SSZ32	86.8	40.8	47.0	13.1	133.8	53.9	1.85	3.12
Pt/SSZ32-0.3A	83.0	35.4	47.8	29.6	130.8	65.0	1.74	1.20
Pt/SSZ32-0.6A	72.5	34.8	53.7	35.4	126.3	70.2	1.35	0.98
Pt/SSZ32-0.3AS	95.5	43.8	39.1	27.9	134.6	71.7	2.44	1.57
Pt/SSZ32-0.6AS	116.1	50.0	32.8	20.2	149.0	70.2	3.54	2.47

The acid properties of different catalysts after alkali and sequential alkali–acid treatment were further characterized by NH_3 -TPD. As shown in Figure 5, there were two peaks of NH_3 desorption at 210–230 °C and 370–440 °C, which are usually assigned to the weak and strong acid sites, respectively [19]. Compared with the Pt/SSZ32 catalyst, the peak at high temperature shifted to a lower temperature for the alkali-treated catalysts, implying the decreased acid strength of the alkali-treated catalysts, especially for Pt/SSZ32-0.6A. However, after the alkali–acid treatment, both the NH_3 desorption peaks shifted toward a higher temperature. This suggested the enhanced overall acid strength of the sequential alkali–acid-treated catalysts, especially for Pt/SSZ32-0.6AS. The acid strength change in these catalysts was ascribed to the reduced framework Al species with the increased extra-framework Al species after NaOH treatment, more exposed framework Al species in the formed mesopore, and the regenerated channels by the removal of extra-framework Al species after further acid treatment. These resulted in the increased acid sites per unit of catalyst mass (Table 3). These results indicated that the Pt/SSZ32-0.6AS catalyst had a stronger acidity strength than other catalysts, which was consistent with the results of Py-FTIR, textual properties, and XRF analysis. The acidity variation changed by the alkali–acid treatment would subsequently have a significant direct impact on the performance of the *n*-hexadecane hydroisomerization process.

**Figure 5.** NH_3 -TPD profiles of parent and hierarchical SSZ-32-supported Pt catalysts.

2.2. Catalytic Hydroisomerization of *n*-Hexadecane over Different Catalysts

The influence of post-treated SSZ-32-zeolite-supported Pt catalysts on the hydroisomerization reaction process was further investigated. The hydroisomerization performance of different catalysts was evaluated using *n*-hexadecane as the model compound in a fixed-bed reactor. As shown in Figure 6, the conversion of *n*-hexadecane over different catalysts gradually increased with the elevating temperature. The Pt/SSZ32 catalyst showed a

high activity for the *n*-hexadecane hydroisomerization with the conversion of ca. 100% at the temperature of 280 °C. Compared with the Pt/SSZ32 catalyst, the conversion of *n*-hexadecane over the alkali-treated catalysts at the same reaction temperature became lower and decreased in the order Pt/SSZ32 > Pt/SSZ32-0.3A > Pt/SSZ32-0.6A. On the contrary, the activity of alkali–acid-treated catalysts was significantly enhanced and became higher than that of the Pt/SSZ32 catalyst. The highest activity was achieved over the Pt/SSZ32-0.6AS catalyst with a relatively low temperature at 260 °C to reach the conversion of 100%. Although the apparent hierarchical structure was generated in the alkali-treated catalysts, the catalytic activity was not enhanced. Obviously, the catalytic activity depended on the total B acidity (Table 3). The Pt/SSZ32-0.3A catalyst showed a similar B acidity with the Pt/SSZ32 catalyst. The similar curve of conversion versus temperature was also obtained over these two catalysts. A much lower activity was obtained on the Pt/SSZ32-0.6A catalyst because of the lowest B acidity, while for the Pt/SSZ32-0.3AS and Pt/SSZ32-0.6AS catalysts, the total B acidity increased more than that of Pt/SSZ32, and, accordingly, the activity became much higher. These results indicated that the total B acidity played the vital role in the hydroisomerization of *n*-alkanes on the bifunctional catalysts, which was consistent with the literature [46,47]. This further proved that the B acid sites participate in the reaction of alkane hydroisomerization, and more B acid sites could enhance *n*-hexadecane protonation to boost the catalytic performance according to the bifunctional catalytic mechanism [32,47]. Of course, the formed mesopore also contributed to providing more accessible acid sites and reducing the diffusion restriction of reactants and/or intermediates, which was also beneficial to improving the catalytic activity.

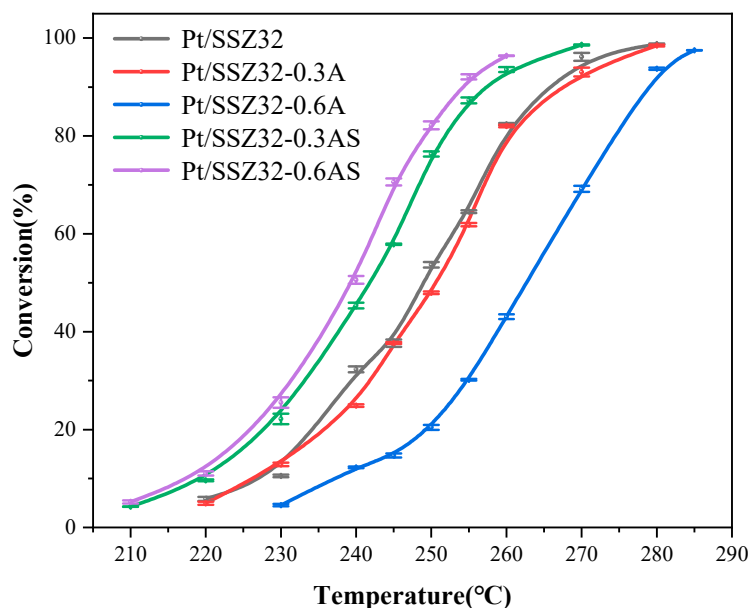


Figure 6. *n*-Hexadecane conversion over parent and hierarchical SSZ-32-supported Pt catalysts.

The yields of total C₁₆ isomers on different catalysts are shown in Figure 7a. The similar yield curves were obtained on all catalysts. As the reaction temperature increased, the yield of *i*-C₁₆ products increased then decreased at high conversion. The highest yield of *i*-C₁₆ products (71.5%) was achieved on the Pt/SSZ32-0.6AS catalyst at 255 °C, while the maximum yield of *i*-C₁₆ products was only 65~68% over other catalysts. In the hydroisomerization of *n*-alkanes, the rearrangement of carbenium ions is the rate-determining step [47]. The rearrangement of carbenium ions can be accelerated with an increase in reaction temperature, resulting in an increase in isomer yield. However, at higher temperature, the hydrocracking of isomers occurred via two types of scission (type A tertiary alkylcarbenium ions intervene, and type B, β-scission) and became severe. Therefore, the yield of isomers decreased. *n*-Hexadecane underwent hydroisomerization

and hydrocracking reactions simultaneously over the bifunctional catalysts, which were competitive reactions. The regulation of the isomerization-cracking equilibrium mainly focuses on the control of the probability of the intermediates meeting with acid sites and the retention time for intermediates over acid sites. The post-treated catalysts showed different catalytic selectivity for the reactions of hydroisomerization and hydrocracking. As shown in Figure 7b, the selectivity of *i*-C₁₆ products decreased gradually with the increase in conversion. As the conversion exceeded 90%, the selectivity of *i*-C₁₆ products dramatically decreased due to the rapid increase in cracking products (Figure 7c). All the catalysts except Pt/SSZ32-0.6A showed a high selectivity of *i*-C₁₆ products over 85%, with the conversion below 80%. The Pt/SSZ32-0.6A catalyst exhibited the lowest selectivity of ca. 80% with the highest cracking product selectivity (ca. 20%). In the conversion of 35–85%, the selectivity of *i*-C₁₆ products decreased over the catalysts as follows: Pt/SSZ32-0.3A > Pt/SSZ32-0.6AS > Pt/SSZ32-0.3AS > Pt/SSZ32 > Pt/SSZ32-0.6A. The yield ratio of isomers to cracking products (*iso*/*C* ratio) was further obtained to compare the influence of post-treatment on the selectivity of two reaction pathways. As shown in Figure 7d, the *iso*/*C* ratio decreased as follows: Pt/SSZ32-0.3A > Pt/SSZ32-0.6AS > Pt/SSZ32-0.3AS > Pt/SSZ32 > Pt/SSZ32-0.6A. These results indicated that the post-treated catalysts, except Pt/SSZ32-0.6A, significantly enhanced the hydroisomerization reaction pathway rather than the cracking reaction pathway. This could be attributed to the variation in Brønsted acidity, especially the weak B acidity. As for the hydroisomerization over different zeolites, a detailed understanding of the reaction mechanism in the presence and/or absence of shape selectivity has been developed by extensive studies with both large-pore zeolites and with medium-pore zeolites [48–52]. According to the reported mechanism of alkane hydroisomerization, the consecutive reaction steps occur on an ideal bifunctional catalyst: *n*-hexadecane ↔ monobranched isohexadecane ↔ multibranched isohexadecane ↔ cracked products. Furthermore, the weak Brønsted acidity is beneficial to the hydroisomerization reaction, while the strong B acidity mainly promotes the excessive isomerism reaction, and the generated multibranched isomeric products are likely to crack, thus, contributing to the cracking reaction [53]. It was speculated that the variation in *iso*/*C* ratios was relative to the change in Brønsted acidity distribution. As listed in Table 3, the alkali treatment caused the decrease of Brønsted acidity for Pt/SSZ32-0.3A and Pt/SSZ32-0.6A. Although more mesopores were generated in Pt/SSZ32-0.6A than in Pt/SSZ32-0.3A, the ratio of weak to strong Brønsted acidity (B_w/B_s) for Pt/SSZ32-0.6A (1.09) became much lower than that for Pt/SSZ32-0.3A (1.35) due to the partial coverage of BAS in the formed hierarchical structure. Moreover, the B_w/B_s ratio for Pt/SSZ32-0.3A was also much higher than that of Pt/SSZ32 (1.13). As shown in Figure 7c, the Pt/SSZ32-0.3A catalyst showed a much higher hydroisomerization selectivity than the Pt/SSZ32 and Pt/SSZ32-0.6A catalysts. This indicated that the reaction pathway selectivity of hydroisomerization and cracking strongly depended on the weak Brønsted acidity distribution of the SSZ-32 zeolite. Compared with Pt/SSZ32-0.3A, the acid-treated Pt/SSZ32-0.3AS catalyst exhibited more and larger mesopores but a lower B_w/B_s ratio (1.18) because of the removal of desilicated Al fragments and the destruction of some framework Al species. In contrary, the Pt/SSZ32-0.6AS showed more mesopores and a higher B_w/B_s ratio (1.32) than that of Pt/SSZ32-0.6A due to the removal of extra-framework Al species. These two catalysts showed higher *iso*/*C* values than the Pt/SSZ32 catalyst. Interestingly, the *iso*/*C* values almost showed a linear increase with the increase in B_w/B_s ratio, as shown in Figure 7d. These results confirmed that the selectivity of the hydroisomerization reaction strongly depended on the B_w/B_s ratio. Different from the reported results, the generated hierarchical structure in the post-treatment had no direct influence on the reaction pathways of hydroisomerization and cracking but could regulate the acidity distribution.

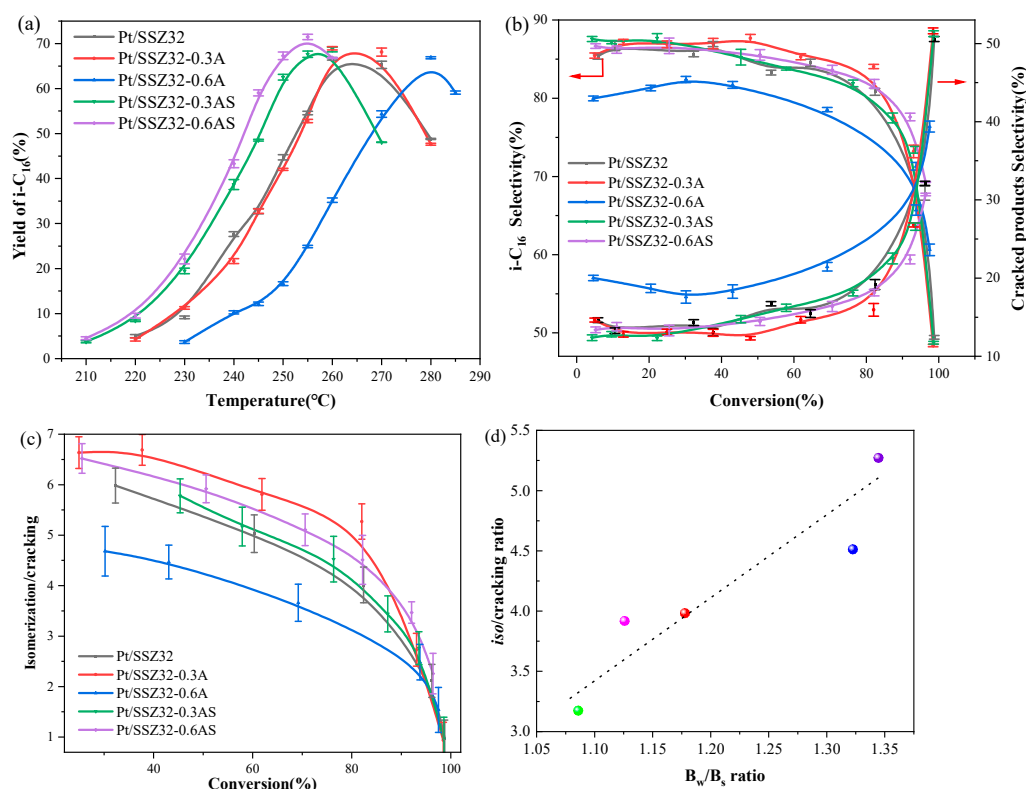


Figure 7. The reaction pathways' selectivity of hydroisomerization and hydrocracking over parent and hierarchical SSZ-32-supported Pt catalysts. (a) Yield of *i*-C₁₆ products; (b) the selectivity of isomers and cracking products; (c) the ratio of isomerization/cracking reaction pathways versus conversion; (d) the iso/cracking ratios at ca. 80% conversion versus B_w/B_s ratios.

As per the aforementioned reaction mechanism, the hydroisomerization of *n*-hexadecane could convert it into the monobranched *i*-C₁₆ products and multibranched *i*-C₁₆ products. The isomer distribution over different catalysts is plotted in Figure 8. All the catalysts showed similar variations in monobranched and multibranched *i*-C₁₆ products. As shown in Figure 8c, the ratio of mono-/multibranched *i*-C₁₆ products was much higher than 1 and decreased linearly with the increase in *n*-C₁₆ conversion. This indicated that the hydrocracking of multibranched isomer occurred similarly on all the catalysts, and the dibranched and tribranched alkanes could not be accommodated by sterical restrictions; thus, monobranched isomers were exclusively formed on these bifunctional catalysts [44]. Compared with the Pt/SSZ32 catalyst, the alkali- and alkali-acid-treated catalysts showed a higher ratio of mono-/multibranched *i*-C₁₆ products, and the ratio decreased in the following order: Pt/SSZ32-0.3A > Pt/SSZ32-0.6A ≈ Pt/SSZ32-0.6AS > Pt/SSZ32-0.3AS > Pt/SSZ32. This result suggests that the formed hierarchical structure dominantly enhanced the selectivity of monobranched *i*-C₁₆ products by enhancing the diffusion of the reactants and intermediates in the bifunctional catalysts. However, comparing the different hierarchical catalysts, it could be inferred that the synergetic effect of hierarchical structure and acidity regulation promoted the selectivity of monobranched *i*-C₁₆ products.

The product distribution of monobranched *i*-C₁₆ products was further analyzed to investigate the reaction mechanisms involved. Figure 9 shows the distribution of 2-,3-,4-, 5- and 6/7/8-methyl isomers. All the catalysts showed the highest selectivity of 2-methyl isomer, probably because this skeletal isomer possessed a minimum diffusion limit [54]. Additionally, high central position branching, such as 6/7/8-methyl isomers, were obtained on all the catalysts. The selectivity of 2-methyl isomer over the Pt/SSZ32, Pt/SSZ-0.3A, and Pt/SSZ-0.6A catalysts decreased gradually from the initial 30% to 20% at the *n*-C₁₆ conversion of 80%. However, for the Pt/SSZ-0.3AS and Pt/SSZ-0.6AS catalysts, the selectivity of 2-methyl isomer decreased gradually from the initial 35% to 25%. At high

conversion (80~100%), the selectivity of 2-methyl isomer showed a rapid decrease to ca. 15%. The total selectivity of 6/7/8-methyl isomers showed an almost linear increase from ca. 32% to 42% with the increase in n -C₁₆ conversion up to 100% at the same time. The selectivity of 3-, 4- and 5-methyl isomers showed almost the same change over the different catalysts. All the catalysts showed a selectivity of 3-methyl isomers of about 15%. About 12% selectivity of 4-methyl isomers was obtained at the conversion below 80% and then gradually increased by about 3% at 100% conversion, while the selectivity of 5-methyl isomers slowly increased at below 80% conversion and then also gradually increased by about 3% at 100% conversion. As reported, the isomer product distributions could be explained by the pore mouth and key-lock modes of physisorption of long n -alkanes in pore openings of the zeolite [54]. The 2- and 3-methyl-branched isomers were more favorably formed via the pore mouth mechanism, and key-lock modes favored the central branching of the chain, such as 6/7/8-methylbranched isomers along the carbon chain [19,54]. To further investigate the influence of post-treatment on the isomerization modes, the typical product distribution at 80% conversion was obtained and listed in Table 4. It can be observed that the yield ratio of 2-/3-methylbranched to 6/7/8-methylbranched isomers (P/K ratio) changed over the different post-treated catalysts. The alkali-treated Pt/SSZ32-0.3A and Pt/SSZ32-0.6A showed almost the same P/K ratios (~0.96) with the Pt/SSZ32 catalyst, indicating that the key-lock mode dominated the formation of monobranched isomers over these catalysts. However, the alkali-acid-treated catalysts exhibited a higher P/K ratio (1.009 for Pt/SSZ32-0.3AS and 1.063 for Pt/SSZ32-0.6AS), indicating that the pore mouth mode became the dominant reaction pathway in the formation of monobranched isomers. This suggests that only alkali-treated catalysts had no influence on the isomerization pathways, but the sequential alkali-acid-treated catalysts could tailor the adsorption mode of isomerization intermediates, probably due to the pore widening and more exposed pore mouth, as well as the more exposed acid sites in the pore mouth.

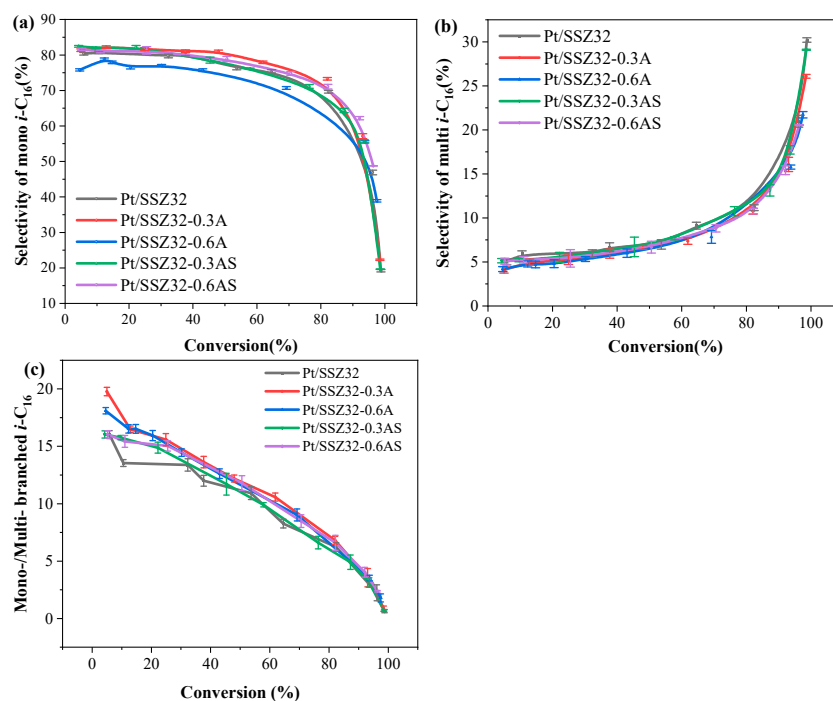


Figure 8. The C₁₆ isomer distribution over different catalysts. (a) The selectivity of monobranched *i*-C₁₆ products; (b) the selectivity of multibranching *i*-C₁₆ products; (c) the ratio of mono- to multi-branched *i*-C₁₆ products.

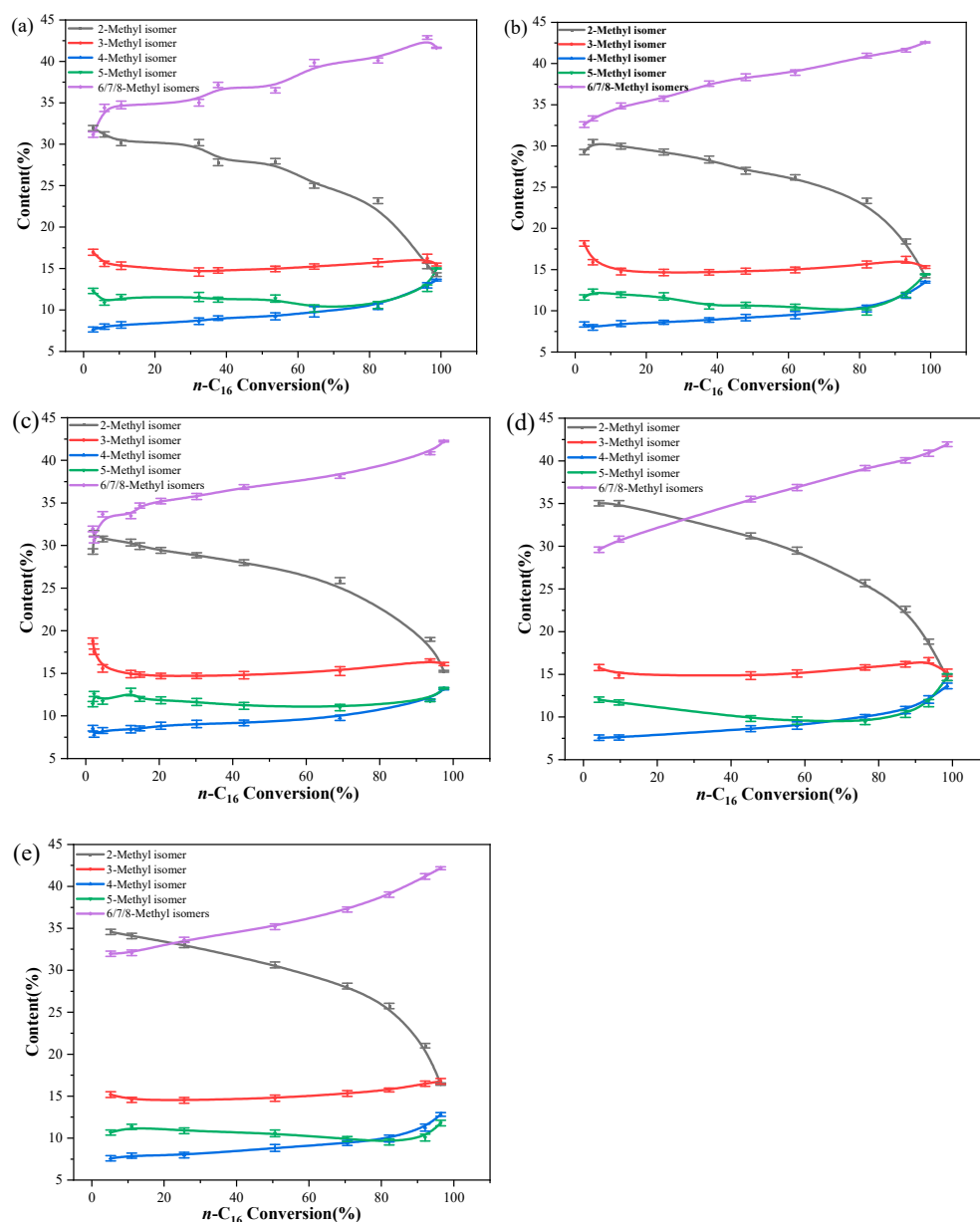


Figure 9. The selectivity of methyl-branched $i\text{-C}_{16}$ isomers versus $n\text{-C}_{16}$ conversion over different catalysts. (a) Pt/SSZ32; (b) Pt/SSZ32-0.3A; (c) Pt/SSZ32-0.6A; (d) Pt/SSZ32-0.3AS; (e) Pt/SSZ32-0.6AS.

Table 4. The product distribution of $n\text{-C}_{16}$ hydroisomerization on different catalysts at the conversion rate of 80%.

$i\text{-C}_{16}$ Products	Yield (%)				
	Pt/SSZ32	Pt/SSZ32-0.3A	Pt/SSZ32-0.6A	Pt/SSZ32-0.3AS	Pt/SSZ32-0.6AS
2-Methyl isomer (pore mouth)	13.30	14.03	11.19	13.27	15.04
3-Methyl isomer (pore mouth)	9.02	9.40	8.07	8.85	9.19
4-Methyl isomer	5.97	6.18	5.52	5.77	5.82
5-Methyl isomer	6.08	5.90	5.78	5.48	5.57
6/7/8-Methyl isomers (key-lock)	23.03	24.62	20.02	21.92	22.80
Pore mouth/key-lock	0.969	0.952	0.962	1.009	1.063

3. Experimental Section

3.1. Catalysts Preparation

3.1.1. Synthesis of Parent SSZ-32

The parent SSZ-32 zeolite used in this work was synthesized by a hydrothermal method according to the literature [18]. First, 1.2 g of *N,N*-diisopropylimidazolium chloride (Acros) was dissolved in 17.6 g of deionized water, and 9.35 g of 1.0 M KOH aqueous solution was added to adjust the pH value. After stirring for 15 min, 5.93 g of Ludox AS-30 (Sigma-Aldrich, Shanghai, China) was added, followed by dropping 1.87 g of Nalco's 1056 colloid sol (Sigma-Aldrich, Shanghai, China) into the mixture. Then, 0.7 g of isobutylamine was added and further stirred for an additional 15 min. The obtained gel was transferred into a Teflon-lined steel autoclave for dynamic crystallization (120 rpm) at 175 °C for 9 days. The product was filtered, washed, and dried at 120 °C for 12 h, and then finally calcined at 595 °C for 5 h.

3.1.2. Synthesis of Hierarchical SSZ-32

The parent SSZ-32 was calcined at 595 °C in air for 5 h before the following treatment. The desilication of SSZ-32 was first carried out. In a typical run, 1 g of SSZ-32 zeolite was mixed with 10 mL NaOH solution (0.3 M, 0.6 M) and heated at 80 °C for 1.5 h under stirring. Subsequently, the obtained slurry was cooled to room temperature, filtered, washed with deionized water to pH = 7.0, and then dried overnight at 120 °C. The resultant zeolites were subjected to continuous ion exchange three times with a 1.0 M NH₄Cl solution at 80 °C for 4 h, filtered, dried, and finally calcined at 550 °C for 4 h. The obtained samples were denoted as SSZ32-*n*A, where *n* represents the concentration of NaOH alkaline solution in desilication.

Then, the sequential dealumination of desilicated SSZ-32 zeolites was further carried out. Part of the above desilicated zeolite was subjected to acid treatment in 0.1 M HNO₃ solution at 80 °C for 6 h with a solid concentration of 20 g L⁻¹. The obtained slurry was cooled to room temperature, filtered, washed with deionized water to be neutral and dried overnight at 120 °C. Then, the resultant zeolites were ion-exchanged three times with NH₄Cl (1.0 M) solution at 80 °C for 4 h and calcined at 550 °C for 4 h to prepare the protonated samples. The obtained samples were denoted as SSZ32-*n*AS.

The parent and as-prepared hierarchical SSZ-32-zeolite-supported 0.5 wt.% Pt catalysts were prepared by an incipient wetness impregnation method using H₂PtCl₆ aqueous solution. The samples were dried overnight at room temperature. Then, the samples were calcined at 450 °C in air for 4 h. Finally, the obtained catalysts loaded with Pt were named Pt/SSZ32, Pt/SSZ32-0.3A, Pt/SSZ32-0.6A, Pt/SSZ32-0.3AS, and Pt/SSZ32-0.6AS, respectively.

3.2. Catalyst Characterization

The phase purity and relative crystallinity of the samples were characterized by X-ray diffraction (XRD) on a D8 advance X-ray diffractometer with (Cu K α) radiation at 40 kV and 140 mA. The morphology and structure of the samples were characterized by field emission scanning electron microscopy (SEM, Hitachi S-4800) and transmission electron microscopy (TEM, Tecnai G2 F20). The pore structure and specific surface area of the catalysts were measured using a Micromeritics Model ASAP 2460 Version 3.01 volumetric instrument. Prior to the test, the samples were degassed at 300 °C for 12 h under vacuum. The Brunauer–Emmett–Teller (BET) method was used to calculate the total specific surface area. The total pore volume of the pores was obtained at $p/p_0 = 0.95$ and the *t*-plot method was used to determine the micropore volume and micropore area. The mesopore size distribution was obtained from the adsorption branch of the isotherm using the Barrett–Joyner–Halenda (BJH) model. The Si and Al content of each sample were determined with an X-ray fluorescence spectrometer (XRF, Supermini200). Pyridine adsorption Fourier transform infrared spectra (Py-IR) was collected on a VERTEX 70 spectrometer (Bruker) in the scanning range of 400–4000 cm⁻¹ to make a distinction between the Lewis (LAS)

and Brønsted (BAS) acid sites. The densities of the Lewis and Brønsted acid sites were calculated by integrating the absorbance at 1545 and 1455 cm^{-1} , respectively, in the py-IR spectra at 200 °C and 350 °C. Temperature-programmed desorption of ammonia (NH_3 -TPD) was carried out with an AMI-300 chemisorption analyzer to measure the total number of acid sites of the samples. Solid-state ^{27}Al magic-angle spinning (MAS) nuclear magnetic resonance spectra (^{27}Al -NMR) were acquired on a Varian Infinity Plus 300 MHz solid-state NMR spectrometer.

3.3. Catalytic Hydroisomerization of *n*-Hexadecane

The hydroisomerization of *n*-C16 was carried out in a down-flow fixed bed (1.0 cm i.d. and 45 cm in length). The reaction temperature was monitored with a thermocouple in the catalyst bed and controlled by three thermocouples on the reactor. Typically, 2 g of the catalysts in 20–40 mesh were loaded into the reactor. Before the reaction, the catalysts were reduced in situ with hydrogen at 400 °C and 3 MPa for 4 h. Then, the reaction was carried out under 260–330 °C at 3 MPa with a $\text{H}_2/n\text{-C16}$ volume ratio of 1000 and weight hourly space velocity (WHSV) of 2.0 h^{-1} . After the reaction became stable, the products were cooled with a heat exchanger and were separated into gas and liquid fractions in a separator. Different liquid samples at an interval of 30 min were collected. The products were qualitatively and quantitatively analyzed by an Agilent 6890 N gas chromatography/5975 N mass spectrometer (GC/MS) and a gas chromatographer (Agilent 7890A GC). The conversion of *n*-hexadecane(*n*-C16) and selectivity of isomers (*i*-C16) were calculated according to [18]. The average results from the three replicated experiments were used.

4. Conclusions

In summary, the hierarchical SSZ-32-zeolite-supported Pt catalysts were prepared by alkali treatment and sequential alkali–acid treatment for *n*-hexadecane hydroisomerization. The hierarchical structure and acidity of support SSZ-32 zeolite were tailored. The sequential acid treatment after alkali treatment generated more mesopore and more Brønsted acidity and increased the B_w/B_s ratio. Compared with Pt/SSZ32(1.13), the Pt/SSZ32-0.3AS and Pt/SSZ32-0.6AS B_w/B_s ratios prepared by sequential alkali–acid treatment were 1.18 and 1.32, respectively. The mesopores generated by post-treatment had nearly no effect on the reaction pathway selectivity of hydroisomerization and cracking. The selectivity on the hydroisomerization reaction strongly depended on the B_w/B_s ratio. The *iso*/*C* values almost had a linear increase with the increase in B_w/B_s ratio. The *iso*/*C* ratio increased as follows: Pt/SSZ32-0.6A(3.17) < Pt/SSZ32(3.92) < Pt/SSZ32-0.3AS(3.98) < Pt/SSZ32-0.6AS(4.51) < Pt/SSZ32-0.3A(5.27); the corresponding B_w/B_s ratio is 1.09, 1.13, 1.18, 1.32, and 1.35, respectively. The synergetic effect of hierarchical structure and acidity regulation promoted the selectivity of monobranched *i*-C₁₆ products. Moreover, the alkali-treated SSZ-32-supported Pt catalysts had no influence on the isomerization mechanism of monobranching via pore mouth or key–lock modes, but the sequential alkali–acid-treated SSZ-32-supported Pt catalysts could enhance the pore mouth mode to form the monobranched *i*-C₁₆ products. This work could provide guidance on designing high-performance bifunctional catalysts and a more comprehensive understanding of the support's roles in the hydroisomerization of long-chain *n*-alkanes. Meanwhile, it also provided an alternative strategy for enhancing the low-temperature performance of diesel or lubricating oils in the petroleum industry.

Author Contributions: X.Y.: investigation, conducting experiments, writing—original draft. W.Z.: investigation, measurement and characterization. L.L.: visualization, methodology, formal analysis. X.N.: formal analysis, data curation. Q.W.: conceptualization, supervision, writing—review and editing, data curation. All authors have read and agreed to the published version of the manuscript.

Funding: This research was funded by National Natural Science Foundation of China [Grant No. 22279088].

Acknowledgments: The financial support by the National Natural Science Foundation of China (Grant No. 22279088) is gratefully acknowledged. The authors would like to thank the workers in Shiyanjia Lab (www.shiyanjia.com (accessed on 31 August 2022)) for the material characterizations.

Conflicts of Interest: The authors declare that they have no known competing financial interests or personal relationships that could have appeared to influence the work reported in this paper.

References

1. Benitez, V.M.; Yori, J.C.; Grau, J.M.; Pieck, C.L.; Vera, C.R. Hydroisomerization and Cracking of n-Octane and n-Hexadecane over Zirconia Catalysts. *Energy Fuels* **2006**, *20*, 422–426. [[CrossRef](#)]
2. Corma, A. Transformation of hydrocarbons on zeolite catalysts. *Catal. Lett.* **1993**, *22*, 33–52. [[CrossRef](#)]
3. Ward, J.A. Hydrocracking processes and catalysts. *Fuel Process. Technol.* **1993**, *35*, 55–85. [[CrossRef](#)]
4. Gao, L.; Shi, Z.Y.; Etim, U.J.; Wu, P.P.; Xing, W.; Zhang, Y.; Bai, P.; Yan, Z.F. Superior catalytic performance of micro-mesoporous Beta-SBA-15 composite with a high indexed isomerization factor in hydroisomerization of n-heptane. *Fuel* **2019**, *252*, 653–665. [[CrossRef](#)]
5. Yu, R.; Tan, Y.; Yao, H.; Xu, Y.; Huang, J.; Zhao, B.; Du, Y.; Hua, Z.; Li, J.; Shi, J. Toward n-Alkane Hydroisomerization Reactions: High-Performance Pt–Al₂O₃/SAPO-11 Single-Atom Catalysts with Nanoscale Separated Metal-Acid Centers and Ultralow Platinum Content. *ACS Appl. Mater. Inter.* **2022**, *14*, 44377–44388. [[CrossRef](#)]
6. García-Pérez, D.; Blanco-Brieva, G.; Alvarez-Galvan, M.C.; Campos-Martin, J.M. Influence of W loading, support type, and preparation method on the performance of zirconia or alumina-supported Pt catalysts for n-dodecane hydroisomerization. *Fuel* **2022**, *319*, 123704. [[CrossRef](#)]
7. Jokar, F.; Alavi, S.M.; Rezaei, M. Investigating the hydroisomerization of n-pentane using Pt supported on ZSM-5, desilicated ZSM-5, and modified ZSM-5/MCM-41. *Fuel* **2022**, *324*, 124511. [[CrossRef](#)]
8. Tan, Y.; Hu, W.; Du, Y.; Li, J. Species and impacts of metal sites over bifunctional catalyst on long chain n-alkane hydroisomerization: A review. *Appl. Catal. A Gen.* **2021**, *611*, 117916. [[CrossRef](#)]
9. Deldari, H. Suitable catalysts for hydroisomerization of long-chain normal paraffins. *Appl. Catal. A Gen.* **2005**, *293*, 1–10. [[CrossRef](#)]
10. Jin, D.; Li, L.; Ye, G.; Ding, H.; Zhao, X.; Zhu, K.; Coppens, M.-O.; Zhou, X. Manipulating the mesostructure of silicoaluminophosphate SAPO-11 via tumbling-assisted, oriented assembly crystallization: A pathway to enhance selectivity in hydroisomerization. *Catal. Sci. Technol.* **2018**, *8*, 5044–5061. [[CrossRef](#)]
11. Niu, P.; Xi, H.; Ren, J.; Lin, M.; Wang, Q.; Chen, X.; Wang, P.; Jia, L.; Hou, B.; Li, D. Micropore blocked core-shell ZSM-22 designed via epitaxial growth with enhanced shape selectivity and high n-dodecane hydroisomerization performance. *Catal. Sci. Technol.* **2018**, *8*, 6407–6419. [[CrossRef](#)]
12. Liu, S.; He, Y.; Zhang, H.; Chen, Z.; Lv, E.; Ren, J.; Yun, Y.; Wen, X.; Li, Y.-W. Design and synthesis of Ga-doped ZSM-22 zeolites as highly selective and stable catalysts for n-dodecane isomerization. *Catal. Sci. Technol.* **2019**, *9*, 2812–2827. [[CrossRef](#)]
13. Li, T.; Wang, W.; Feng, Z.; Bai, X.; Su, X.; Yang, L.; Jia, G.; Guo, C.; Wu, W. The hydroisomerization of n-hexane over highly selective Pd/ZSM-22 bifunctional catalysts: The improvements of metal-acid balance by room temperature electron reduction method. *Fuel* **2020**, *272*, 117717. [[CrossRef](#)]
14. Niu, P.; Xi, H.; Ren, J.; Lin, M.; Wang, Q.; Jia, L.; Hou, B.; Li, D. High selectivity for n-dodecane hydroisomerization over highly siliceous ZSM-22 with low Pt loading. *Catal. Sci. Technol.* **2017**, *7*, 5055–5068. [[CrossRef](#)]
15. Woo Lee, S.; Ki Ihm, S. Hydroisomerization and hydrocracking over platinum loaded ZSM-23 catalysts in the presence of sulfur and nitrogen compounds for the dewaxing of diesel fuel. *Fuel* **2014**, *134*, 237–243. [[CrossRef](#)]
16. Zhang, M.; Chen, Y.; Wang, L.; Zhang, Q.; Tsang, C.-W.; Liang, C. Shape Selectivity in Hydroisomerization of Hexadecane over Pt Supported on 10-Ring Zeolites: ZSM-22, ZSM-23, ZSM-35, and ZSM-48. *Ind. Eng. Chem. Res.* **2016**, *55*, 6069–6078. [[CrossRef](#)]
17. Zhang, M.; Li, C.; Chen, Y.; Tsang, C.-W.; Zhang, Q.; Liang, C. Hydroisomerization of hexadecane over platinum supported on EU-1/ZSM-48 intergrowth zeolite catalysts. *Catal. Sci. Technol.* **2016**, *6*, 8016–8023. [[CrossRef](#)]
18. Liu, L.; Zhang, M.; Wang, L.; Zhang, X.; Li, G. Construction of ordered mesopores outside MTT zeolite for efficient hydroisomerization. *Appl. Catal. A Gen.* **2020**, *602*, 117664. [[CrossRef](#)]
19. Liu, L.; Zhang, M.; Wang, L.; Zhang, X.; Li, G. Modulating acid site distribution in MTT channels for controllable hydroisomerization of long-chain n-alkanes. *Fuel Process. Technol.* **2023**, *241*, 107605. [[CrossRef](#)]
20. Wang, X.; Zhang, X.; Wang, Q. N-dodecane hydroisomerization over Pt/ZSM-22: Controllable microporous Brønsted acidity distribution and shape-selectivity. *Appl. Catal. A Gen.* **2020**, *590*, 117335. [[CrossRef](#)]
21. Maesen, T.; Schenk, M.; Vlugt, T.; Jonge, J.; Smit, B. The Shape Selectivity of Paraffin Hydroconversion on TON-, MTT-, and AEL-Type Sieves. *J. Catal.* **1999**, *188*, 403–412. [[CrossRef](#)]
22. Lv, G.; Wang, C.; Wang, P.; Sun, L.; Liu, H.; Qu, W.; Wang, D.; Ma, H.; Tian, Z. Pt/ZSM-22 with Partially Filled Micropore Channels as Excellent Shape-Selective Hydroisomerization Catalyst. *ChemCatChem* **2019**, *11*, 1431–1436. [[CrossRef](#)]
23. Ahmed, M.H.M.; Muraza, O.; Al-Amer, A.M.; Yamani, Z.H. Investigation of crucial synthesis parameters of rich Al-MTT framework zeolite: Toward more determination for synthesis zone of SSZ-32. *Microporous Mesoporous Mater.* **2016**, *227*, 48–56. [[CrossRef](#)]

24. Ojo, A.F.; Lei, G.; Zhang, Y.; Krishna, K.R. Processes for Producing Diesel from Unconventional Feedstocks. U.S. Patent 2,022,204,867-A1, 30 June 2022.
25. Dai, X.; Cheng, Y.; Si, M.; Wei, Q.; Chen, D.; Huang, W.; Zhou, Y. SAPO-11 molecular sieves synthesized in alcohol-water concentrated gel system with improved acidity, mesoporous volume and hydroisomerization performance. *Fuel* **2022**, *314*, 123131. [[CrossRef](#)]
26. Chen, Y.; Li, C.; Chen, X.; Liu, Y.; Liang, C. Synthesis of ZSM-23 zeolite with dual structure directing agents for hydroisomerization of n-hexadecane. *Microporous Mesoporous Mater.* **2018**, *268*, 216–224. [[CrossRef](#)]
27. Chen, Y.; Li, C.; Chen, X.; Liu, Y.; Tsang, C.-W.; Liang, C. Synthesis and Characterization of Iron-Substituted ZSM-23 Zeolite Catalysts with Highly Selective Hydroisomerization of n-Hexadecane. *Ind. Eng. Chem. Res.* **2018**, *57*, 13721–13730. [[CrossRef](#)]
28. Chen, L.-H.; Sun, M.-H.; Wang, Z.; Yang, W.; Xie, Z.; Su, B.-L. Hierarchically Structured Zeolites: From Design to Application. *Chem. Rev.* **2020**, *120*, 11194–11294. [[CrossRef](#)]
29. Serrano, D.P.; Escola, J.M.; Pizarro, P. Synthesis strategies in the search for hierarchical zeolites. *Chem. Soc. Rev.* **2013**, *42*, 4004–4035. [[CrossRef](#)]
30. Verboekend, D.; Pérez-Ramírez, J. Design of hierarchical zeolite catalysts by desilication. *Catal. Sci. Technol.* **2011**, *1*, 879–890. [[CrossRef](#)]
31. Silaghi, M.-C.; Chizallet, C.; Raybaud, P. Challenges on molecular aspects of dealumination and desilication of zeolites. *Microporous Mesoporous Mater.* **2014**, *191*, 82–96. [[CrossRef](#)]
32. Bai, D.; Meng, J.; Li, C.; Zhang, M.; Liang, C. Mesoporosity and Acidity Manipulation in ZSM-23 and their n-Hexadecane Hydroisomerization Performance. *Chemistryselect* **2022**, *7*, e202200839. [[CrossRef](#)]
33. Guo, K.; Ma, A.; Wang, Z.; Li, J.; Wu, B.; Liu, T.; Li, D. Investigation of n-heptane hydroisomerization over alkali-acid-treated hierarchical Pt/ZSM-22 zeolites. *New J. Chem.* **2022**, *46*, 16752–16763. [[CrossRef](#)]
34. Zhou, Q.M.; Wang, S.; Wu, Z.W.; Qin, Z.F.; Dong, M.; Wang, J.G.; Fan, W.B. Aromatization of n-C7–n-C9 alkanes on a Pt/KZSM-5(deAl) catalyst. *Catal. Sci. Technol.* **2023**, *13*, 1009. [[CrossRef](#)]
35. Wang, H.Y.; Zhang, X.W.; Li, G.Z. Constructing optimally hierarchical HY zeolite for the synthesis of high-energy-density tricyclic hydrocarbon fuel. *Mol. Catal.* **2023**, *535*, 112871. [[CrossRef](#)]
36. Mihályi, R.M.; Kollár, M.; Király, P.; Karoly, Z.; Mavrodinova, V. Effect of extra-framework Al formed by successive steaming and acid leaching of zeolite MCM-22 on its structure and catalytic performance. *Appl. Catal. A Gen.* **2012**, *417*, 76–86. [[CrossRef](#)]
37. Thommes, M.; Kaneko, K.; Neimark, A.V.; Olivier, J.P.; Rodriguez-Reinoso, F.; Rouquerol, J.; Sing, K.S. Physisorption of gases, with special reference to the evaluation of surface area and pore size distribution (IUPAC Technical Report). *Pure Appl. Chem.* **2015**, *87*, 1051–1069. [[CrossRef](#)]
38. Groen, J.C.; Moulijn, J.A.; Perez-Ramirez, J. Desilication: On the controlled generation of mesoporosity in MFI zeolites. *J. Mater. Chem.* **2006**, *16*, 2121–2131. [[CrossRef](#)]
39. Chen, K.; Horstmeier, S.; Nguyen, V.T.; Wang, B.; Crossley, S.P.; Pham, T.; Gan, Z.; Hung, I.; White, J.L. Structure and Catalytic Characterization of a Second Framework Al(IV) Site in Zeolite Catalysts Revealed by NMR at 35.2 T. *J. Am. Chem. Soc.* **2020**, *142*, 7514–7523. [[CrossRef](#)] [[PubMed](#)]
40. Yi, X.; Liu, K.; Chen, W.; Li, J.; Xu, S.; Li, C.; Xiao, Y.; Liu, H.; Guo, X.; Liu, S.-B.; et al. Origin and Structural Characteristics of Tri-coordinated Extra-framework Aluminum Species in Dealuminated Zeolites. *J. Am. Chem. Soc.* **2018**, *140*, 10764–10774. [[CrossRef](#)] [[PubMed](#)]
41. Liu, R.; Fan, B.; Zhi, Y.; Liu, C.; Xu, S.; Yu, Z.; Liu, Z. Dynamic Evolution of Aluminum Coordination Environments in Mordenite Zeolite and Their Role in the Dimethyl Ether (DME) Carbonylation Reaction. *Angew. Chem. Int. Edit.* **2022**, *61*, e202210658.
42. Ravenelle, R.M.; Schüßler, F.; D' Amico, A.; Danilina, N.; van Bokhoven, J.A.; Lercher, J.A.; Jones, C.W.; Sievers, C. Stability of Zeolites in Hot Liquid Water. *J. Phys. Chem. C* **2010**, *114*, 19582–19595. [[CrossRef](#)]
43. van Donk, S.; Bitter, J.H.; Verberckmoes, A.; Versluijs-Helder, M.; Broersma, A.; de Jong, K.P. Physicochemical characterization of porous materials: Spatially resolved accessibility of zeolite crystals. *Angew. Chem. Int. Edit.* **2005**, *44*, 1360–1363. [[CrossRef](#)] [[PubMed](#)]
44. Ravi, M.; Sushkevich, V.L.; van Bokhoven, J.A. On the location of Lewis acidic aluminum in zeolite mordenite and the role of framework-associated aluminum in mediating the switch between Brønsted and Lewis acidity. *Chem. Sci.* **2021**, *12*, 4094–4103. [[CrossRef](#)]
45. Ravi, M.; Sushkevich, V.L.; van Bokhoven, J.A. Towards a better understanding of Lewis acidic aluminium in zeolites. *Nat. Mater.* **2020**, *19*, 1047–1056. [[CrossRef](#)] [[PubMed](#)]
46. Palčić, A.; Valtchev, V. Analysis and control of acid sites in zeolites. *Appl. Catal. A Gen.* **2020**, *606*, 117795. [[CrossRef](#)]
47. Ono, Y. A survey of the mechanism in catalytic isomerization of alkanes. *Catal. Today* **2003**, *81*, 3–16. [[CrossRef](#)]
48. Campelo, J.M.; Lafont, F.; Marinas, J.M. Comparison of the activity and selectivity of Pt/SAPO-5 and Pt/SAPO-11 in n-hexane and n-heptane hydroconversion. *Appl. Catal. A Gen.* **1997**, *152*, 53–62. [[CrossRef](#)]
49. Blomsma, E.; Martens, J.A.; Jacobs, P.A. Reaction Mechanisms of Isomerization and Cracking of Heptane on Pd/H-Beta Zeolite. *J. Catal.* **1995**, *155*, 141–147. [[CrossRef](#)]
50. Paul, Z.; Zhan, Z.; Manninger, I.; Sachtler, W.M.H. Skeletal Reactions of n-Hexane over Pt-NaY, Pt/SiO₂, Hy, and Mixed Pt/SiO₂ + HY Catalysts. *J. Catal.* **1995**, *155*, 43–51. [[CrossRef](#)]

51. Martens, J.A.; Jacobs, P.A.; Weitkamp, J. Attempts to rationalize the distribution of hydrocracked products. II. Relative rates of primary hydrocracking modes of long chain paraffins in open zeolites. *Appl. Catal.* **1986**, *20*, 283–303. [[CrossRef](#)]
52. Parton, R.; Uytterhoeven, L.; Martens, J.A.; Jacobs, P.A.; Froment, G.F. Synergism of ZSM-22 and Y zeolites in the bifunctional conversion of n-alkanes. *Appl. Catal.* **1991**, *76*, 131–142. [[CrossRef](#)]
53. Alvarez, F.; Ribeiro, F.R.; Perot, G.; Thomazeau, C.; Guisnet, M. Hydroisomerization and Hydrocracking of Alkanes: 7. Influence of the Balance between Acid and Hydrogenating Functions on the Transformation of n-Decane on PtHY Catalysts. *J. Catal.* **1996**, *162*, 179–189. [[CrossRef](#)]
54. Claude, M.C.; Martens, J.A. Monomethyl-Branching of Long n-Alkanes in the Range from Decane to Tetracosane on Pt/H-ZSM-22 Bifunctional Catalyst. *J. Catal.* **2000**, *190*, 39–48. [[CrossRef](#)]

Disclaimer/Publisher’s Note: The statements, opinions and data contained in all publications are solely those of the individual author(s) and contributor(s) and not of MDPI and/or the editor(s). MDPI and/or the editor(s) disclaim responsibility for any injury to people or property resulting from any ideas, methods, instructions or products referred to in the content.